PCCP

$CuZrO_3$: If it exists it should be a sandwich

Journal:	*Physical Chemistry Chemical Physics*
Manuscript ID	CP-ART-05-2021-002245.R1
Article Type:	Paper
Date Submitted by the Author:	04-Oct-2021

Complete List of Authors:	Dean, James; University of Pittsburgh, Chemical & Petroleum Engineering Yang, Yahui; University of Pittsburgh, Chemical and Petroleum Engineering Veser, Götz; University of Pittsburgh, Department of Chemical and Petroleum Engineering Mpourmpakis, Giannis; University of Pittsburgh, Chemical and Petroleum Engineering

$CuZrO_3$: If it exists it should be a sandwich

James Dean, Yahui Yang, Götz Veser, Giannis Mpourmpakis*

Department of Chemical Engineering, University of Pittsburgh, Pittsburgh PA 15213, USA

Abstract

$CuZrO_3$ has been hypothesized to be a catalytic material with potential applications for CO_2 reduction. Unfortunately, this material has received limited attention in literature, and to the best of our knowledge the exact crystal structure is still unknown. To address this challenge, we utilize several different structural prediction techniques in concert, including the Universal Structure Predictor: Evolutionary Xtallography (USPEX), the Materials Project Structure Predictor, and the Open Quantum Materials Database (OQMD). Leveraging these structural prediction techniques in conjunction with Density-Functional Theory (DFT) calculations, we determine a possible structure for $CuZrO_3$, which resembles a "sandwich" morphology. Our calculations reveal that this new structure is significantly lower in energy than a previously hypothesized perovskite structure, albeit it still has a thermodynamic preference to decompose into CuO and ZrO_2. In addition, we experimentally tried to synthesize $CuZrO_3$ based on literature reports and compared computational to experimental X-ray Diffraction (XRD) patterns confirming that the final product is a mixture of CuO and ZrO_2. Finally, we conducted a computational surface energetics and CO_2 adsorption study on our discovered sandwich morphology, demonstrating that CO_2 can adsorb and activate on the material. However, these CO_2 adsorption results deviate from previously reported results further confirming that the $CuZrO_3$ is a metastable form and may not be experimentally accessible as a well-mixed oxide, since phase segregation to CuO and ZrO_2 is preferred. Taken together, our combined computational and experimental study provides evidence that the synthesis of $CuZrO_3$ is extremely difficult and if this oxide exists, it should have a sandwich-like morphology.

*Corresponding Author Email: gmpourmp@pitt.edu

Introduction

Copper Zirconate was first synthesized in 1832 through the reaction of copper and zirconium salts with ammonia[1, 2]. After this initial synthesis, it would take over a century for interest in the material to re-emerge. Motivated by the tunability of mixed-oxides for different applications, in 1980 Reddy et al[3] conducted the first modern synthesis of $CuZrO_3$. Notably, the first evidence of $CuZrO_3$ as a novel CO_2 adsorber emerged in this work, with adsorbed CO_2 being detected via IR spectroscopy[3, 4]. Based on XRD and the orthorhombic crystal structure of the chemically similar perovskite $BaZrO_3$, Reddy et al hypothesized that the crystal structure was that of a perovskite with an orthorhombic crystal cell.

Recently rekindled interest in perovskite catalysis motivated further studies[5] in the applications of $CuZrO_3$. Saha and Hamid[6] synthesized $CuZrO_3$ nanoparticles (NPs) to catalyze the aerobic oxidation of vanillyl alcohol. They confirmed the XRD pattern of $CuZrO_3$, and suggested the perovskite structure is distorted, concluding that the high catalytic activity of the material could have resulted from an appreciable number of surface defects. Ehsan et al[7] developed a thin-film deposition technique for 1:1 $CuZrO_3$:CuO. Borhade et al[8] studied $CuZrO_3$ as a dye photodegradation catalyst. Lu et al[9] synthesized $CuZrO_3$ NPs to form a composite with graphene, noting excellent low-concentration detection of Pb(II) and Cd(II) ions in soil, suggesting this results from synergistic effects between the graphene and $CuZrO_3$.

As work with $CuZrO_3$ was being performed, other researchers focused on other, related oxides of CuZr. Fisher and Bell[10] investigated the CO_2 methanation activity of $Cu/ZrO_2/SiO_2$, uncovering a synergistic effect of the H_2 dissociation capability of Cu providing a feedstock for methanation over ZrO_2 regions of the catalyst. Austin et al[11] found Zr-doped Cu NPs to strongly adsorb CO_2, and Dean et al[12] found these Zr-doped Cu NPs to strongly adsorb CO_2 even when oxidized. Aritani et al[13] investigated several mixed oxides for the decomposition of NO with CH_4, finding that a 2wt% Cu/ZrO_2 catalyst had the highest activity among the various catalysts investigated. Furthermore, Liu et al[14] studied various loadings of CuO/tet-ZrO_2 for the catalytic reduction of N_2O to N_2, demonstrating that the catalytic activity correlates with the dispersion of CuO, and observing that Cu ions contribute to most of the activity. Restivo and de Mello-Castanho[15] synthesized a Cu-doped Ni / yttria-stabilized Zr cermet, identifying $CuZrO_3$ as a contaminant.

Our previous work[12] computationally identified that Zr-doped Cu NPs may be potential CO_2 hydrogenation catalysts, based on their predicted adsorption and activation of CO_2. This motivated the synthesis of these particles, and we observed the production of $CuZrO_3$ NPs, which is likely the result of the highly oxophilic nature of Cu and Zr. We further modeled CO_2 adsorption on Zr-oxide patches on pure Cu NPs using DFT, verifying the experimentally observed CO_2 adsorption on $CuZrO_3$ NPs. However, in this study there was a materials gap between theory and experiments due to the lack of crystal structure determination of this material, and a lack of a set of atomic coordinates for $CuZrO_3$. Ultimately, the absence of a known structure for $CuZrO_3$ creates several difficulties: most computational chemistry approaches – which use chemical structure as an input – require much more guesswork if a structure is not known, and without knowledge of the crystal structure it is hard to make definitive conclusions about the nature of any catalytically-active sites on the surface. This motivates our present work: leveraging DFT, modern structural prediction methods and experiments, we aim to shed light onto the structure, stability and adsorption properties of $CuZrO_3$.

Computational and Experimental Methods

Sample Preparation

$CuZrO_3$ was prepared by thermal decomposition of copper zirconyl oxalate which was described by Reddy et al.[3, 16] In brief, equimolar (0.5 M each) aqueous solutions of copper chloride (Sigma Aldrich, ≥99.995%) and zirconyl chloride octahydrate (Sigma Aldrich, 98%) were added to preheated oxalic acid at 60ºC (1.0 M) (Sigma Aldrich, ≥99%) which was 10% in excess. The precipitate was aged for 30 min under mixing. The product was then filtered, washed with distilled water and acetone, and air dried.

The thermal decomposition reaction of the resulting sample (copper zirconyl oxalate) from above procedure was studied by thermogravimetric analysis (TGA) (SDT Q600, TA instruments). The sample (approximately 30 mg) was loaded into the instrument and heated to 950ºC in air flow with a ramp rate of 7ºC/min. We observed weight loss at three temperature ranges above 200ºC (i.e. 200 – 330ºC, 530 – 600ºC and 870 – 900ºC; the weight loss below 200ºC is attributed to dehydration which is not included in the discussion). Based on our observation, we calcined the sample at 800ºC in air (0.2 SLM) for 4 hours with a ramp rate of 7ºC/min. The calcined samples were used to collect XRD pattern.

X-ray Diffraction

The sample crystal structure was measured by Bruker D8 X-ray Diffraction system at 40 kV and 40 mA with Cu Kα radiation (λ = 1.5406 Å) at a scan speed of 0.3 s/step from 10 to 90º.

Density-Functional Theory

We utilize the Vienna Ab-initio Simulation Package (VASP)[17] in conjunction with the PBE functional and PAW potentials[18]. Unless otherwise specified (as in USPEX), we use the following settings for our calculations. A gamma-centered mesh of 5x5x5 k-points is used for bulk systems, and a gamma-centered mesh of 5x5x1 k-points is used for periodic slabs. A planewave cutoff of 500 eV is used, with an SCF convergence criterion of 10^{-5} eV. Geometry optimizations are performed with a convergence criterion of 10^{-4} eV/ Å. Gaussian smearing is used with a width of 0.01 eV.

USPEX Calculations

For USPEX calculations, we optimize unit cells in a series of 5 stages ramping up from 400 eV to a 600 eV cutoff. We also ramp up from k-space resolution of 0.2 to 0.6 $\frac{2\pi}{\text{Å}}$. Gaussian smearing with widths ranging from 0.1 to 0.01 is used across the five stages of optimization. Each generation's population consists of 30 unit cells, keeping the fittest 60% of the previous generation. Fitness is determined as the energy of the structure, scaled by number of formula units in the unit cell. When the same structure ranks as the fittest for 8 consecutive generations, the USPEX calculation is halted.

Materials Project Structure Predictor

For structures generated via the Materials Project Structural Predictor[19, 20], the application requires users to select a guess for the atomic oxidation states. The oxidation states a user is allowed to select are the +1, +2, or +3 state for Cu, -2 for O, and +2, +3, or +4 for Zr. In order to maintain a neutrally charged $CuZrO_3$ system, we can therefore either choose Cu^{2+} with Zr^{4+} or we can choose Cu^{3+} and Zr^{4+}. We chose Cu^{2+} and Zr^{4+} as the oxidation states because Cu is more electronegative

than Zr^{21}, and because these states are more common than the Cu^{3+} and Zr^{3+} states[22, 23]. Additionally, in our prior work synthesizing $CuZrO_3$ NPs[12], we observed the presence of Cu^{2+}, Zr^{4+} via X-Ray Photoelectron Spectroscopy (XPS), partially-reduced $Zr^{(4-x)+}$ species, as well as, the lack of any Cu^{3+} or Zr^{3+} ions.

Unit Cell Optimization

A variety of techniques for the ab-initio prediction of crystal structure have arisen in the last decade. In this work, we utilize the genetic algorithm USPEX, the probabilistic Structure Prediction tool of Materials Project, and the OQMD in order to get a set of potential structures for $CuZrO_3$. We additionally take the crystal structure of the mineral perovskite, $CaTiO_3$ to be part of our set of possible structures.

Once we have generated a structure guess, we optimize the unit cell by first scanning volumes ranging from 0.4 to 2 times the initial unit cell. We then take the volume minimizing the energy and perform a geometry optimization of the atomic coordinates only. Then, we allow atomic coordinates and unit cell parameters to vary at a constant volume. In the final stage of optimization, we allow the atomic coordinates, unit cell parameters, and volume to all vary.

Slab and Adsorption Calculations

To calculate surface energies, we cleave along the respective Miller index, and freeze the centermost layer of the slab (to facilitate a symmetrically-relaxed surface). Only surface terminations where both sides are equivalent through mirror or glide-plane symmetry are investigated. A slab thickness of 3 (i.e. a frozen center layer is flanked by 1 unfrozen layer on both sides, for a total of 3 layers) is used. A vacuum of 10 Å is used in the calculations. In addition, we use a gamma-centered 5x5x1 set of k-points. Surface energies (σ) are calculated via Equation 1, with E_{slab} being the DFT-calculated energy of the slab, E_{cell} being the DFT-calculated energy of the unit cell, A being the area of one side of the slab, n_{slab} being the number of formula units in the slab, and n_{cell} being the number of formula units in the unit cell.

$$\sigma = \frac{E_{slab} - \left(\frac{n_{slab}}{n_{cell}}\right) E_{cell}}{2A} \quad (1)$$

For adsorption calculations, we cleave the bulk along the respective Miller index, freeze the bottom layer of the slab, and relax the other atoms. We then place a CO_2 molecule in a potential binding site initially in an activated (bent) state. In both cases, we apply an automatic dipole correction along the axis perpendicular to the slab. In addition, for this set of calculations, we increased the vacuum size to 15 Å. We calculate the binding energy (E_{bind}) of CO_2 to the slab using Equation 2, where $E_{complex}$ is the DFT energy of the slab with CO_2 attached, and E_{CO2} is the DFT energy of a single CO_2 molecule.

$$E_{bind} = E_{complex} - E_{slab} - E_{CO_2} \quad (2)$$

Cells for XRD Prediction

XRD predictions are generated using VESTA[24], with the same wavelength as our experimental XRD work. For each unit cell, the peak intensities are then scaled such that they have the same maximum as our experimentally determined XRD. The same wavelength used in the experimental XRD work is used to parameterize VESTA's predictions.

Bader Analysis

The Bader method[25] was used to calculate the charges in the fully-optimized structures (see the "Unit Cell Optimization" section). VASP was set to write the all-electron charge densities to file and VASP Transition State Tools (VTST) were used to sum the core density and self-consistent valence densities reported by VASP. This result was then used as the reference charge ("-ref" option) for the Bader analysis.

Finally, the net charge of each ion was calculated by subtracting the Bader-calculated population from the number of valence electrons specified in the PAW pseudopotential (11 for Cu, 12 for Zr, and 6 for O).

Results and Discussion

We start our study by generating candidate structures for $CuZrO_3$. A perovskite unit cell contains metal atoms at two possible sites, generally known as the "A" and "B" site (see Figure 1)[26]. The A-site is a coordination number (CN) 12 site, and the B site is a CN 6 site surrounded by an electronegative species (typically a halogen or chalcogen).

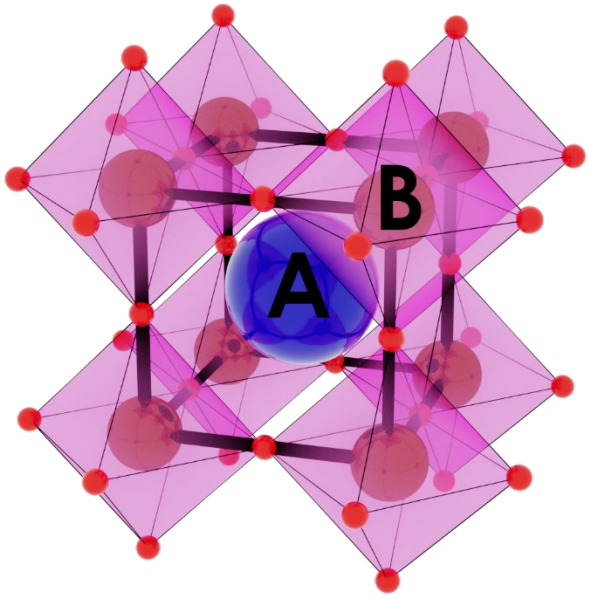

Figure 1. An ideal perovskite unit cell. The blue atom represents the A-site, and the purple atoms / polyhedra represent the B-site. Halogen/chalcogen atoms are shown in red, at the tips of the octahedra. The unit cell for this system is illustrated by the thick black lines extended between the B-site cations.

Empirical relations exist which allow one to estimate whether a set of elements will form a perovskite. The Goldschmidt tolerance factor[27] is a well-known relation which can help predict whether a compound with formula XYZ_3 will form a perovskite. X and Y are the two cations, typically metals, and Z is the anion. Because the exact crystal structure of $CuZrO_3$ is unknown, we

consider two cases: one where Zr is in the A-site (with Cu in the B-site) and one where Cu is in the A-site (with Zr being in the B-site).

We applied the Goldschmidt tolerance factor to both scenarios (see Supporting Information section Structural Tolerance Factors), and found that in either case, a perovskite is predicted. In the case where Zr is in the A-site and Cu is in the B-site, the Goldschmidt tolerance factor is 0.82, which indicates an orthorhombic perovskite. In the case where Cu is in the A-site and Zr is in the B-site, the Goldschmidt tolerance factor is 0.87, which also indicates a perovskite.

One drawback to the Goldschmidt tolerance factor is a high false-positive rate, which was addressed in a new perovskite tolerance factor recently developed by Bartel et al[28]. Compared with the Goldschmidt tolerance factor, this improved tolerance factor was demonstrated to reduce the false-positive rate from 51% to just 11%, while simultaneously increasing the true-positive rate from 74% to 92%. Thus, Bartel's tolerance factor is less likely to mis-identify a material as a perovskite when it is not, and more-likely to correctly identify a material as a perovskite when it is. The tolerance factor τ predicts a material to be a perovskite when $\tau < 4.18$ (see Supporting Information section Structural Tolerance Factors). In the case where Zr^{4+} is in the A-site, this results in $\tau = 1.13$, which indicates a perovskite. In the case where Cu^{2+} is in the A-site, however, $\tau = 4.45$, which is high enough to predict that a perovskite would not occur.

Overall, both the Goldschmidt and Bartel tolerance give evidence that $CuZrO_3$ may form a perovskite, however the Bartel tolerance factor yields the possibility that one may not form. The work of Reddy et al[3] hypothesized that the material forms a perovskite, and Saha and Hamid[6] suggest that the structure is a distorted perovskite. All this prior work justifies narrowing down our search to the materials space encompassing only structures which are similar to perovskites.

A logical first guess is to generate a prototype structure from the mineral perovskite ($CaTiO_3$). These cells use the experimental unit cell parameters of $CuZrO_3$ for their unit cell parameters. Because there are a variety of ways the unit cell parameters could be oriented (i.e. the question of which axis in the cell is the shortest/longest), we investigate every possible combination of unit cell vectors, for a total of 6 initial unit cells. In addition, because the Goldschmidt tolerance factor indicates that either Cu or Zr could be in the A-site (with the other residing in the B-site), we investigate both cases. This yields a total of 12 perovskite-derived prototypes.

The Open Quantum Materials Database (OQMD)[29, 30] is a large corpus of high-quality DFT calculations. The database also performs automated structure generation, with perovskite structures being investigated for many ABO_3-type materials. The database has a perovskite $CuZrO_3$ structure derived from $SrFeO_3$ with either Cu or Zr in the octahedra, so this yields a total of 2 structure guesses.

The Materials Project Structure Predictor[19, 20] is a probabilistic model which predicts the structure of hypothetical materials. At a high-level, it operates by creating a new crystal structure based on chemical similarity with other known structures. For example, because Ca and Ba are chemically similar ions, one may expect $BaTiO_3$ to have similar structure to $CaTiO_3$ (perovskite) – and $BaTiO_3$ indeed forms a perovskite unit cell. We use this model to predict several structures for $CuZrO_3$, again using the assigned charges Cu^{2+}, O^{2-}, and Zr^{4+}. Since multiple structures are returned, we take the three most probable structures based on the ranking by the Structure Predictor (which is based on a data-mined tendency for two ions to swap locations, resulting in a crystal of the desired formula). In addition to these structures, we consider the two next highest-probability perovskite-like structures. This yields a total of 5 structure guesses.

The Universal Structure Predictor: Evolutionary Xtallography (USPEX)[31-33] is a highly successful genetic algorithm which attempts to optimize a population of potential crystal structures, with the objective function of minimizing the energy of the cell. It interfaces readily with VASP with minimal setup. Also, other groups have investigated similar systems using USPEX. These include the pressure-composition phase diagram of ZrO_2[34] (parameterized with VASP) and a study which involved the prediction of several experimentally-known crystal structures including CuO and Cu_2O[35] (parameterized with CRYSTAL17[36]).

To search in parallel, three calculations are conducted simultaneously: one checking unit cells ranging between 1 and 4 formula units, one between 4 and 6 formula units, and one between 7 and 8 formula units. This yields a total of 3 structure guesses. The preceding 22 structure guesses were optimized in VASP. The 5 lowest-energy structures are reported in Table 1. The energies of all optimized structure can be found in the Supporting Information. In addition, using the same DFT methodology, we optimized the structure of pure CuO and ZrO_2 to assess the thermodynamic stability of each $CuZrO_3$ cell against decomposition into the two oxides. The decomposition energy of the $CuZrO3 \rightarrow CuO + ZrO_2$ reaction is determined via Equation 3. In each case, energy is relative to the number of formula units.

$$E_{Decomp} = \left(E_{CuO} + E_{ZrO_2}\right) - E_{CuZrO_3} \qquad (3)$$

Table 1. Electronic energies of the five lowest-energy unit cells (E_{cell}) for $CuZrO_3$ found in this study. Energetics for all structure guesses can be found in Supporting Information Table S3. The decomposition energies (E_{decomp}) are also presented for the reaction $CuZrO3 \rightarrow CuO + ZrO_2$. Our reference energy for the CuO system is -9.83 eV/formula unit. Our reference energy for the ZrO_2 system is -28.78 eV/formula unit.

Structure	Number of Formula Units	E_{cell} (eV/Formula Unit)	E_{decomp} (eV/Formula Unit)
USPEX-ea430 (Sandwich)	2	-38.19	-0.42
USPEX-ea480	4	-37.94	-0.68
Perovskite Prototype (Zr Oct)-D	4	-37.91	-0.70
Materials Project-1140859	4	-37.83	-0.79
Perovskite Prototype (Cu Oct)-B	4	-37.77	-0.84

Of interest is that the "Perovskite Prototype" is not the most favorable structure. We note that over the course of the optimization, this system has deviated from the perovskite structure (see Supporting Information section "Deviation from the Perovskite Prototype" for more details). In the "Perovskite Prototype" system, we find that the A-site Cu cation migrates to the 4-fold planar coordinated sites present along the edges of the B-site Zr octahedra (see Supporting Information Figure S3 D), yielding a decomposition energy of -0.70 eV/formula unit. For the purposes of discussion and to be consistent in our naming scheme, we will continue to refer to this system as the "Perovskite Prototype," although we should note here that it is not actually a perovskite at the end of the optimization.

Moreover, the OQMD structural prototypes retained their perovskite structure during optimization, yet had the two strongest decomposition energies (e.g. decomposition is strongly favored) over all the systems we have investigated: -3.56 eV/formula unit when Cu is the A-site cation, and -5.28 eV/formula unit when Zr is the A-site cation (see Supporting Information Table S3).

The most stable structure we find, the USPEX-ea430 structure, has a decomposition energy of -0.42 eV/formula unit. The UPEX-ea430 system exhibits thin layers of Cu atoms tetra-coordinated with O sandwiched between thick layers of slightly distorted Zr octahedra. As a result, we label this the "sandwich" morphology. Interestingly, despite being the most energetically favorable unit cell, the sandwich morphology still favorably decomposes (-0.42 eV/formula unit) to CuO and ZrO_2. This helps in rationalizing the presence of CuO[3, 6] and ZrO_2[6, 9] reported in several syntheses of $CuZrO_3$. The sandwich morphology (Figure 2) has a nearly orthorhombic unit cell with side lengths $a = 3.96, b = 3.96, c = 8.52,$ and angles $\alpha = 90.0°, \beta = 102.1°, \gamma = 90.0°$. As reference, the true unit cell is orthorhombic with side lengths $a = 6.45, b = 7.40, c = 8.31$.

If we produce a 2x2x1 supercell of the sandwich morphology, the side lengths are relatively close to the true unit cell, at $a = 7.92, b = 7.93, c = 8.52$. To test the effect of this deviation in unit cell dimensions, we constrained the unit cell dimensions of the 2x2x1 supercell to the experimental dimensions of $CuZrO_3$. With this constraint in place, we then relaxed just the atomic coordinates. This resulted in an electronic energy of -37.10 eV/formula unit and a decomposition energy of -1.51 eV/formula unit, thus showing an even-more energetically favorable decomposition to CuO and ZrO_2.

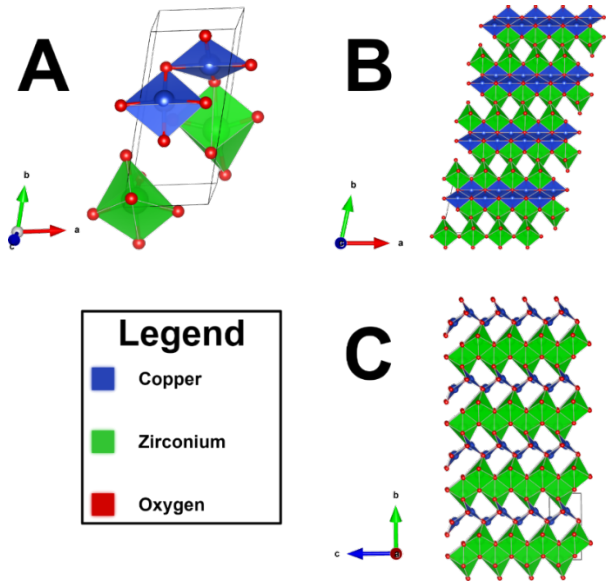

Figure 2. Sandwich morphology. (A) bulk unit cell. (B) 4x4x4 supercell looking down the pores present in the Zr octahedra. (C) 4x4x4 supercell looking down the pores present at the interface between the Zr octahedra and Cu quadrilaterals. The unit cell in all cases is drawn with black lines. Key: Blue=Cu, Green=Zr, Red=O.

We note that there is some degree of structural similarity between the sandwich morphology and the unit cells for CuO and monoclinic ZrO_2 (Figure 3). We can see a "ladder" of alternating Zr-O bonds extending through the ZrO_2 cell (Figure 3 A), which also exists as a structural component

of the oxidized Zr phase of the $CuZrO_3$ sandwich (Figure 3 B). In the cell for CuO (Figure 3 C), there are two sets of strips of square-planar CuO units, which are perpendicular to one-another and joined at the edge. In our $CuZrO_3$ unit cell (Figure 3 D), we retain the morphology of having two sets of CuO squares – albeit seesaw shapes connected at the vertices, instead of square planes connected at the edges.

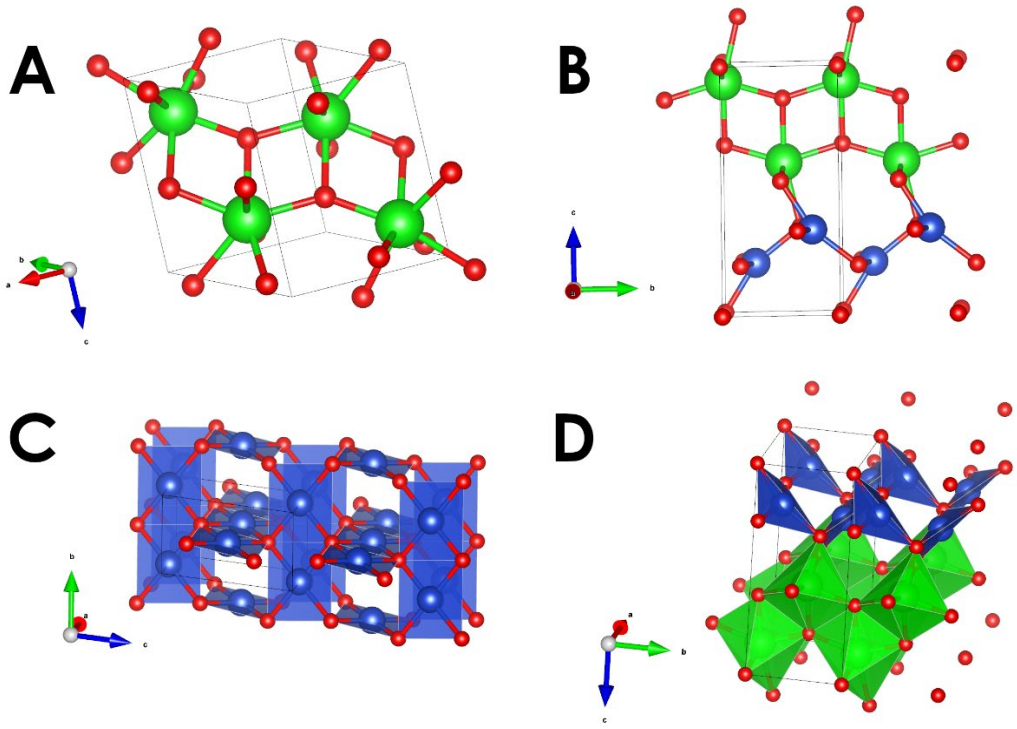

Figure 3. Comparison of monoclinic ZrO_2 (A) and CuO (C) with the $CuZrO_3$ sandwich structure (B and D). Key: Blue=Cu, Green=Zr, Red=O.

Part of this may be due to the size of the unit cells we considered, where a unit cell was able to contain at most 7 formula units of $CuZrO_3$ – a limit we chose for computational tractability reasons. Ultimately, if $CuZrO_3$ is unstable with a favorable decomposition into CuO and ZrO_2, a genetic-algorithm-based optimization strategy may find better solutions for larger cells by maximizing the segregation of the oxidized Cu and oxidized Zr phases.

To further characterize the structure of $CuZrO_3$, we have also leveraged Bader analysis[25] on the VASP-calculated charges of our system (Figure 4). We observe negatively-charged oxygens (slightly more negative than -1), positively charged Cu (+1 in both cases), and more-positive Zr (+2.56 in both cases). In the case of Zr, it is pertinent to refer back to our prior work on model $CuZrO_4$ NPs[12], where we had calculated the oxidized Zr patch (Zr had been surrounded by 4 oxygens) to possess a charge of +2.3. Of interest is that, even in the case of our prior model $CuZrO_4$ NP, and in the case of the sandwich morphology, Zr does not possess a +4 charge, but instead +2.3 (prior work[12]) and +2.56 (this work). This is, however, very close to the charge of +2.6 we calculate on Zr atoms in ZrO_2. As a result, this charge transfer is indicative of a +4 oxidation state of Zr.

In our prior work's XPS component, we had observed the presence of a partially reduced ($Zr^{(4-x)+}$) species in addition to Zr^{4+}. Briefly, recall our calculations suggesting a favorable decomposition into CuO and ZrO_2 for all structures found so far, including the perovskite structure that had been

suggested in the initial synthesis of $CuZrO_3$[3]. In addition, we find that even in the lowest-energy structure, there is not any variation in the oxidation states between the Zr atoms. This may suggest that the true structure of $CuZrO_3$ may indeed be metastable, and that what had been experimentally observed may have been the result of a decomposition into CuO and ZrO_2, with possibly some doping between them.

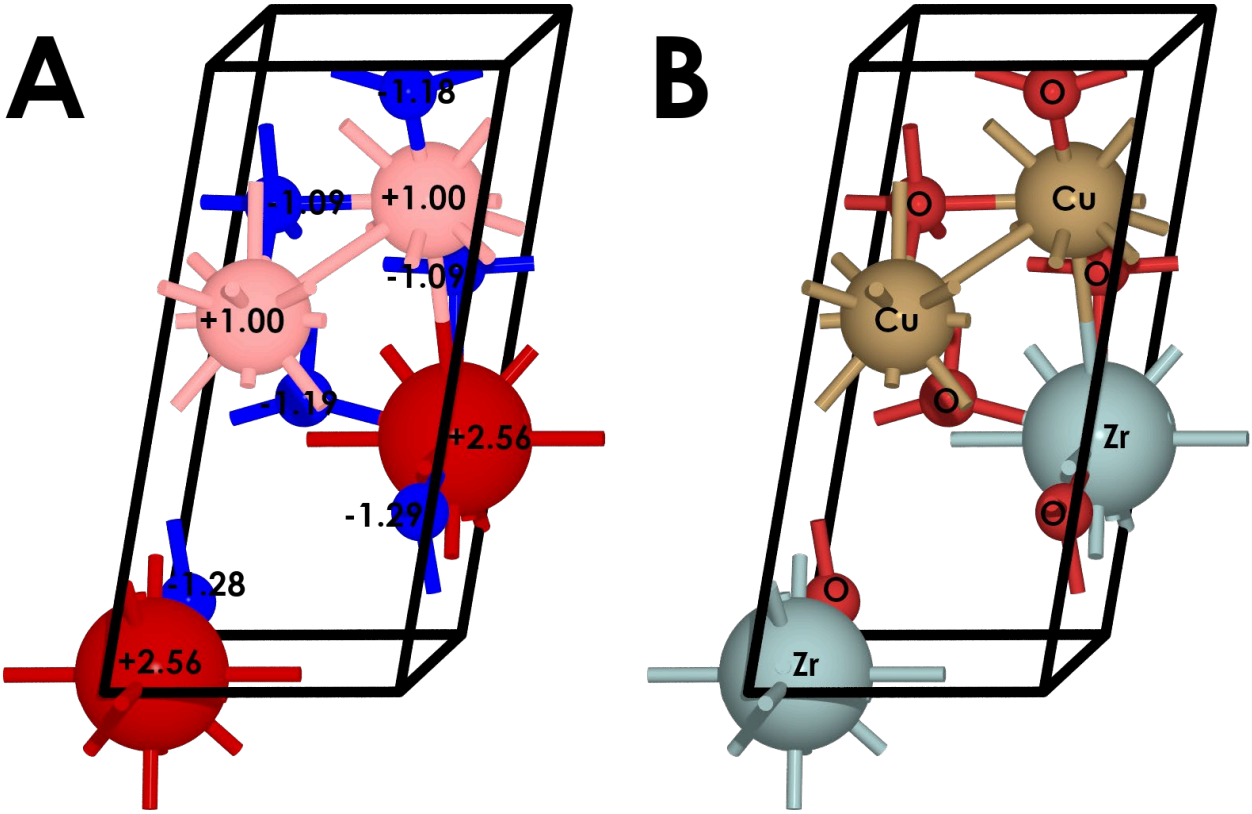

Figure 4. Charge analysis of the $CuZrO_3$ sandwich morphology. (A) Bader-calculated charges, with each atom colored and labeled by its charge. Key: Blue=negatively charged, Red=positively charged. (B) Model of the $CuZrO_3$ sandwich morphology, rotated in the same manner for comparison, with each atom colored and labeled by its atomic symbol. Key: Brown=Cu, Light blue=Zr, Red=O."

Additionally, we further performed PBE0[37] single point energy calculations and we confirmed the decomposition preference of both structures to their parent oxides, albeit with a competition of the Perovskite Prototype structure as a metastable structure (see Supporting Information section "PBE0 Comparison"). A limited geometry optimization further revealed a flip in this trend, with the sandwich structure again becoming more favorable than the "perovskite prototype" (which we re-iterate, unlike the OQMD structures, had ceased being a perovskite during the PBE optimization process). Further optimization calculations with hybrid functionals may shed further light into the exact energetic stability of the metastable structures.

To support our computational work, we experimentally prepared a sample of $CuZrO_3$ per the synthetic technique of Reddy et al.[3] We then conducted an XRD study at 800 °C, drawing our resulting pattern as a solid black line in Figure 5. The peaks reported by Reddy et al are drawn as red lines. The close agreement between the diffraction patterns confirms that we successfully

reproduced the $CuZrO_3$ synthesis by Reddy et al[3, 16]. The XRD result is also in good agreement with the XRD analysis of Ehsan et al[7].

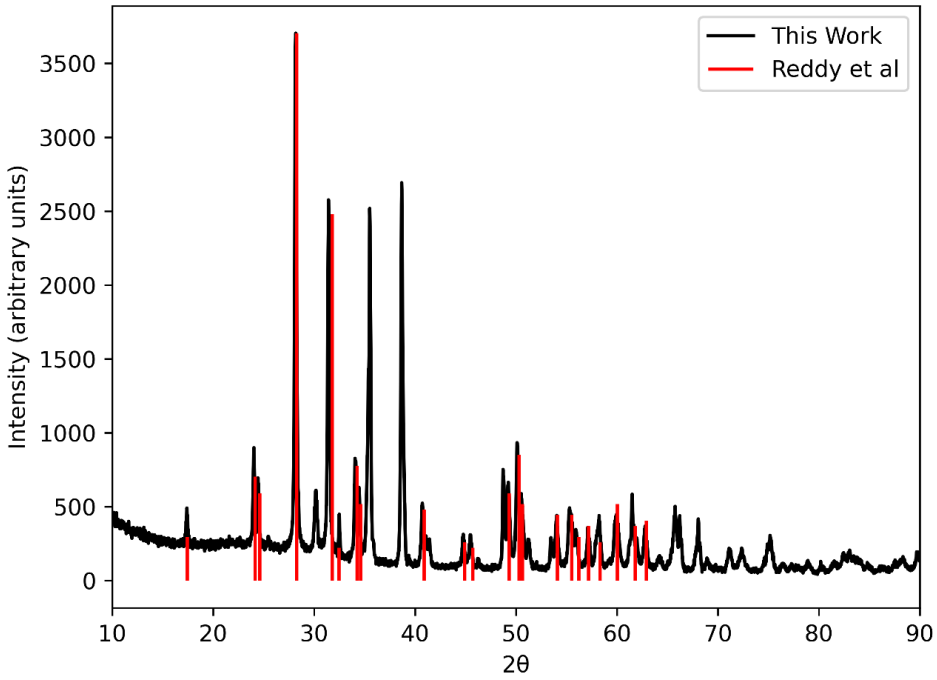

Figure 5. Comparison between our synthesized $CuZrO_3$ sample at 800 ºC (black), the peaks reported in the original synthesis by Reddy et al[3] (red). To facilitate comparison, the XRD intensities reported by Reddy et al are scaled such that their maximum intensity is the same as our sample's maximum intensity.

In addition to our experimental XRD, we show in Figure 6A the XRD pattern for an idealized perovskite cell, with unit cell parameters equal to the known values for $CuZrO_3$. Additionally, in Figure 6B, we take the 2x2x1 unit cell of the sandwich morphology and calculate its XRD pattern after scaling the unit cell parameters to the experimental unit cell parameters.

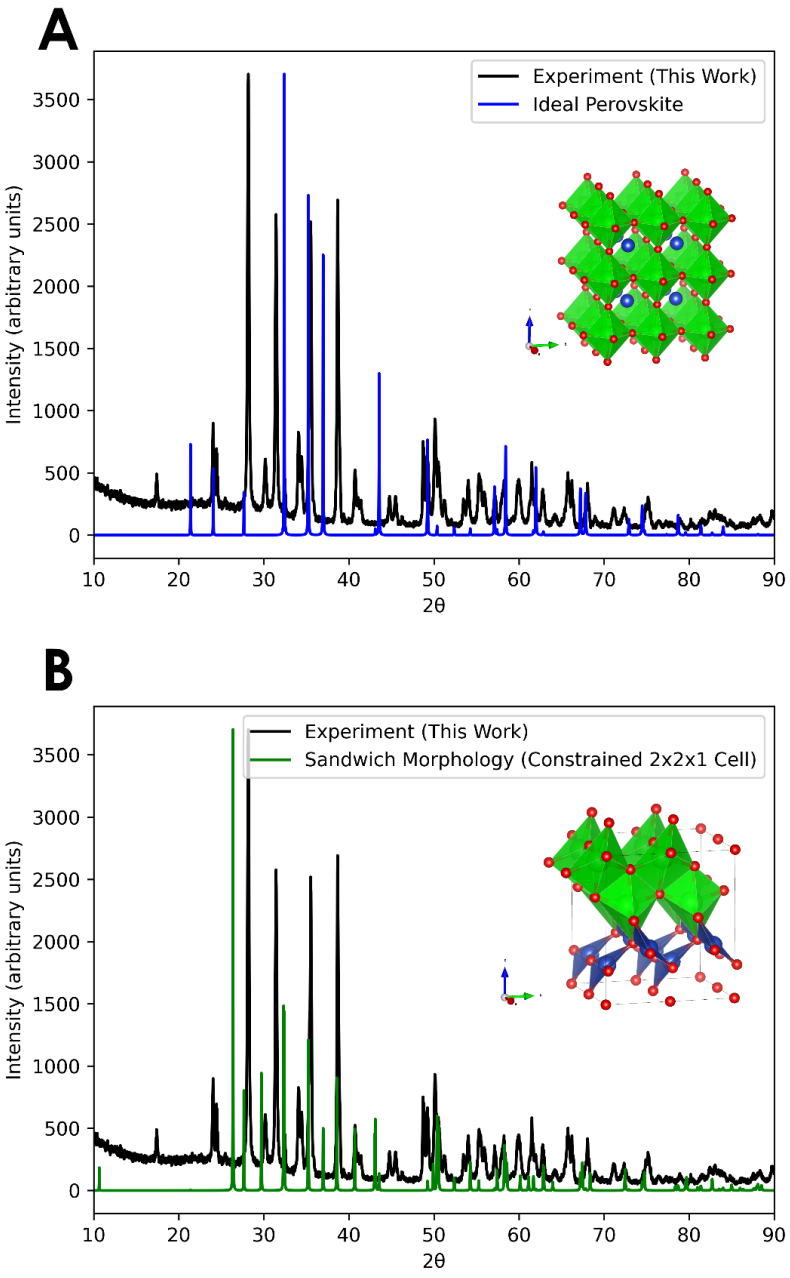

Figure 6. Comparison of XRD for our synthesized $CuZrO_3$ sample at 800 ºC (black) and two possible candidates for $CuZrO_3$. A) Idealized perovskite morphology. B) 2x2x1 supercell of the sandwich morphology (green) suggested in this work. Both predicted XRD intensities are scaled such that their maximum corresponds with our synthesized sample's maximum intensity, and an image of the unit cell being used to calculate the pattern is included as an inset. In both cases, the cell parameters are set such that they are equal to the known unit cell dimensions.

Overall, the results suggest that $CuZrO_3$ has an unstable crystal structure. Even for the most energetically favorable structure we found (the sandwich morphology, see Table 1), decomposition to CuO and ZrO_2 is favored. In addition, our predicted XRD patterns for either structure of $CuZrO_3$ do not agree well with the experimental pattern (Figure 6). A careful analysis of the XRD diffractogram in Figure 5 shows that most of the peaks can be attributed to CuO and ZrO_2 (as demonstrated in our previous CO_2 adsorption study[12] involving $CuZrO_3$ NPs), suggesting decomposition of the structure into CuO and ZrO_2. We note that this also explains some of the differences between the simulated spectra and the experimental spectrum. In the case of the simulated spectra, a single pure phase of either unit cell is assumed, in contrast with the experimental results, which have decomposition products present.

Nonetheless, in our prior study, we detected CO_2 adsorption energetics that could not be explained by CuO, ZrO_2, or the SiC support, suggesting that they originated from a $CuZrO_3$ mixed-oxide phase. To better understand this experimental observation, we hence turn to the most favorable candidate for $CuZrO_3$ that we identified: the sandwich morphology which, from an energetic standpoint, is much more favorable than even the perovskite structure.

To this end, we investigated the 001, 100, and 101 surface facets of a 2x2x1 supercell of the sandwich morphology, because they are both low-Miller-index surfaces and have symmetric terminations. In the case of 001, and 100, two symmetric surface terminations (which we name A and B) were identified. Symmetric terminations for the 100 surface can be found in Figure 7. Surface energies for all terminations are reported in Table 2. We observe that the 100 surface is the energetically most favorable, followed closely by the 001 surface (Table 2). Since the 100 A-termination has the most favorable surface energy, it was adopted for our subsequent adsorption work. This slab is relatively narrow in one direction and to avoid the adsorbate from interacting with itself, we used a 2x1 supercell of the slab.

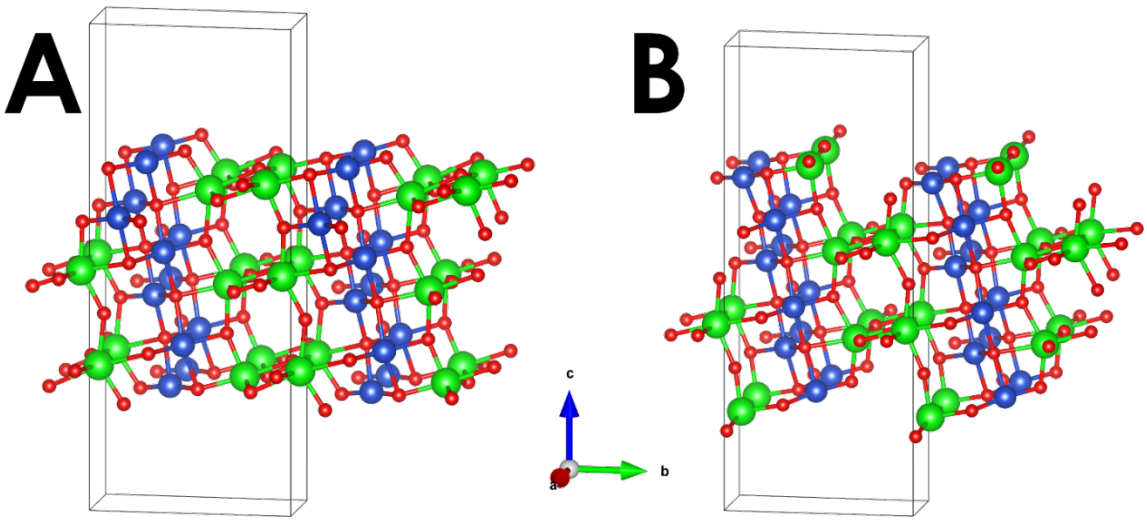

Figure 7. DFT-optimized structures of the two symmetric terminations identified for the 100 surface. (A) Termination A. (B) Termination B. Key: Blue=Cu, Green=Zr, Red=O.

Table 2. Surface energies for sandwich morphology in J/m^2.

Facet	Termination	Surface Energy (J/m^2)
101	A	1.36
100	A	0.85
100	B	1.20
001	A	1.08
001	B	0.99

We investigated the adsorption of CO_2 to 6 surface sites on the A-termination of the 100 plane (Figure 8). In every case, to facilitate convergence to strongly adsorbed states, we place CO_2 molecules in a pre-activated position. From the 6 adsorption configurations in Figure 8, we observe CO_2 to converge to only 3 types of adsorption configuration, shown in Figure 9. Configurations A, B, and E in Figure 8 converge to an almost linear CO_2 state with $\angle_{OCO} = 176°$ (Figure 9 A). Configuration C in Figure 8 converges to a physisorbed state (Figure 9 B). Finally, configurations D and F result in the formation of a chemisorbed and activated (bent) species (Figure 9 C). In the case of Figure 8 D and F, CO_2 remains whichever side of Cu it is initially placed, and we report that which is lower in energy in Figure 9 C.

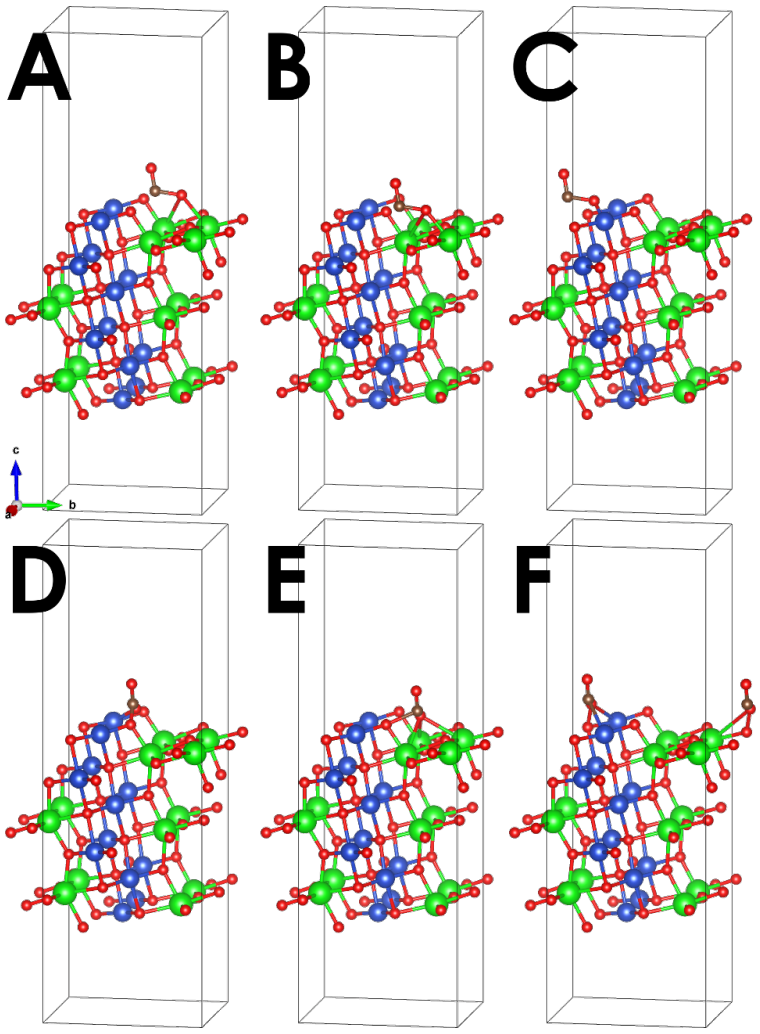

Figure 8. Initial adsorption configurations on the 100 A-termination. An axis indicating cell vector directions is drawn in subfigure A. Key: Blue=Cu, Green=Zr, Red=O, Black=C.

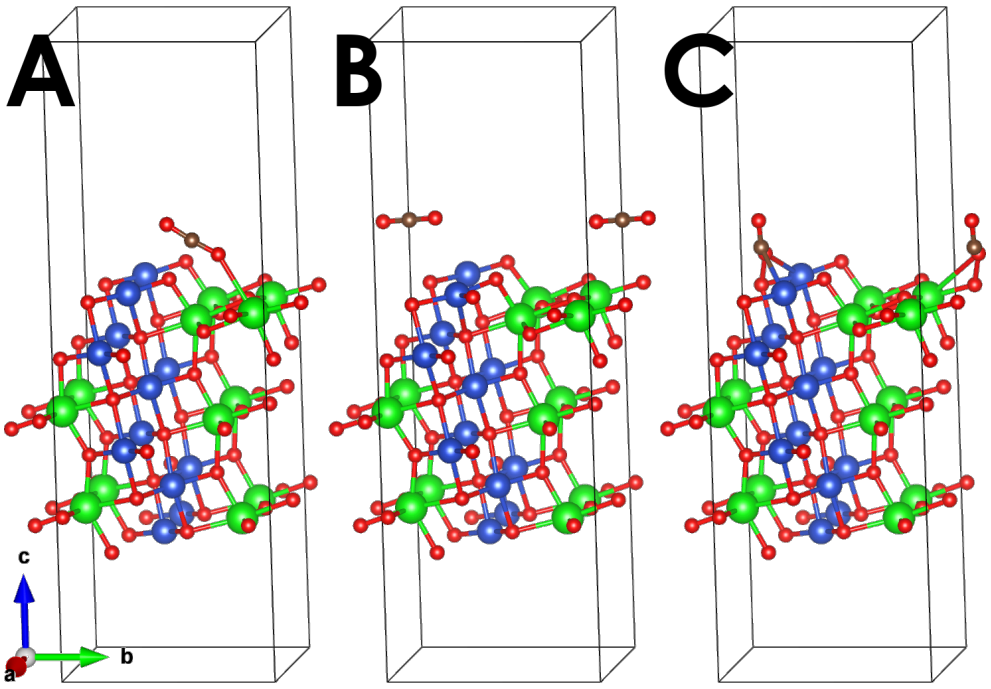

Figure 9. Final (optimized) adsorption configurations on the 100 A-termination. A) Almost linear CO_2. B) Physisorbed CO_2. C) Activated CO_2. Labels in this figure correspond to those in Table 3. An axis indicating cell vector directions is drawn in subfigure A. Key: Blue=Cu, Green=Zr, Red=O, Black=C.

These three configurations show a range of adsorption energies (Table 3). An almost linear configuration of CO_2 (Figure 9 A, Table 3 A) adsorbs strongly at -0.45 eV. The weakly bound, linear CO_2 (Figure 9 B, Table 3 B) physisorbs with energy -0.17 eV. Finally, CO_2 (Figure 9 C, Table 3 C) binds in an activated state, at -0.19 eV. It should be noticed that the CO_2 adsorption configuration presented in Figure 9 A has the oxygen of CO_2 coordinating with surface Zr (an oxophilic atom). This is an important observation since this strongly bound conformation of CO_2 is observed on surface Zr atoms that do not necessarily activate the molecule (i.e. the decrease in bond angle is very slight). In contrast, Cu-O sites (Figure 9 C) appear to activate CO_2, while exhibiting lower adsorption energy compared to the Zr site.

Table 3. Adsorption energies for CO_2 on the 100 A-termination. Adsorption configuration labelling corresponds with that of Figure 9.

Adsorption Configuration (*Figure 9*)	**DFT Adsorption Energy (eV)**	**DFT+D3 Singlepoint Adsorption Energy (eV)**
A	-0.45	-0.55
B	-0.17	-0.18
C	-0.19	-0.24

These energies are weaker than the experimental results of our prior work[12], which reported desorption energies ranging from -0.99 to -1.23 eV. A potential cause of this could be the neglect of dispersion contributions, which may play a significant role in the case of CO_2. To check whether this is indeed a source of error, we calculate the binding energy by running single-point calculations of the CO_2, bare surface, and CO_2-surface systems (Table 3). We observe an enhanced binding energy in all 3 cases, but the resulting energies are not within the previous experimental observations.

We additionally attempted to relax the surface using PBE+D3, i.e. repeat this adsorption study with dispersion, but we were unable to converge the geometry for several structures. Instead, we froze the atoms of the slab in place, and allowed just CO_2 to relax – this facilitated convergence of the geometry. This was performed for each of the 3 configurations depicted in Figure 9 and Table 3, and the converged structures are reported in Figure 10. In all three cases, we start from the same initial geometries used for Figure 9, i.e. CO_2 starts near the surface in a pre-activated state.

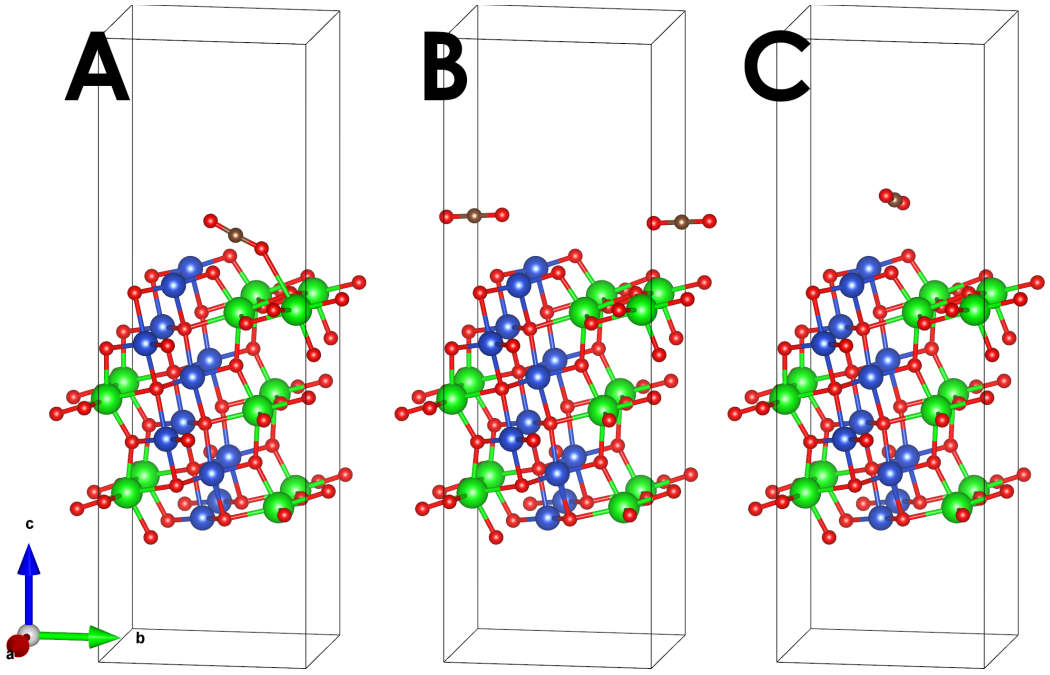

Figure 10. Final (optimized) adsorption configurations on the 100 A-termination, when PBE+D3 is used, and only CO_2 is allowed to relax (i.e. the entire slab is frozen). A) Nearly-linear physisorbed CO_2. B) Physisorbed CO_2. C) Physisorbed CO_2.

Structure A (Figure 10A) converged to nearly the same final state reported in Figure 9A, with the $\angle_{OCO}$ increasing by one degree to 177°. Structure B (Figure 10B) converges to the same physisorbed structure reported in Figure 9B. Interestingly, structure C (Figure 10C) no longer converges to an activated structure (which was the case in Figure 9C). Instead, it converges to a physisorbed state. The adsorption energies were again similar (Table 4), with the largest change being a weakening of structure A's adsorption energy by 0.1 eV. Overall, despite the dispersion correction, the results are hence still not in good agreement with our previously reported experimental results[12].

Table 4. Adsorption energies for the 100 A-termination when the D3 correction is applied. Labels in the first column correspond to the labels used in Figure 10.

Adsorption Configuration (*Figure 10*)	**DFT+D3 Adsorption Energy**
A	-0.47
B	-0.15
C	-0.18

This discrepancy is surprising, given that a singly-doped NP model in our original study[12] was able to reflect the experimentally observed strong CO_2 adsorption much more accurately. Specifically, in that work we observed that model systems consisting of an oxidized Zr patch doped on an otherwise-monometallic Cu NP reproduced the experimental results well. We note that our previous XPS results had shown the presence of Zr^{4+}, Cu^{2+}, and Cu^0 species, and that TEM images confirmed the presence of pure (metallic) Cu NPs. Considering that a model system which has an oxidized patch of Zr on an otherwise-metallic Cu NP is able to reproduce the experimental results better than a model system with fully-oxidized Zr and Cu species, it may be reasonable to infer that the strong CO_2 adsorption energies may result from the interface of an oxidized Zr^{4+} phase, formed from the decomposition of $CuZrO_3$, and a metallic Cu^0 phase, rather than from a true mixed oxide phase. Indeed, it is known that interfacial effects play an important role in CO_2 hydrogenation on Cu/ZrO_2 catalysts[38, 39]. We also note that the doping of Cu into a ZrO_2 phase is a possibility, as several works[40, 41] have investigated the doping of ZrO_2 systems with Cu, including one which investigated a Cu-doped ZrO_2 aerogel for the hydrogenation of CO to CH_3OH[42]. Another explanation could be different surface terminations (high-energy surfaces reported in Table 2) or, most likely, surface hydroxyl groups that result in the formation of bicarbonate species that could bind CO_2 stronger[12]. Future studies should focus on the surface hydration of this new structure, as well as the interface with other phases (such as Cu).

Conclusions

Taking stock of the body of work on $CuZrO_3$, we address a current gap in literature: to the best of our knowledge, there is no set of atomic coordinates available for this material. We confirm that the Goldschmidt[27] and Bartel[28] tolerance factors predict the formation of a perovskite material, which is consistent with prior characterization work[3, 6]. Leveraging several structural prediction strategies including USPEX[31-33], the Materials Project Structure Predictor[19, 20], and the OQMD[29, 30], we find that the perovskite, which is the generally accepted structure of $CuZrO_3$, does not appear to be the lowest-energy structure within the framework of PBE DFT. Moreover, even the lowest-energy structure we identified appears to have a thermodynamically favorable decomposition to CuO and ZrO_2. This is in agreement with the X-ray diffraction pattern of the material which can be explained based only on the presence of CuO and ZrO_2, respectively. Taking the lowest-energy structure, we investigate several potential surfaces, and identify that the 100 surface as the most-stable. CO_2 adsorption energy calculations then show that CO_2 can adsorb and activate on the surface. However, these CO_2 adsorption results are different from previously reported experimental studies, providing further evidence that the $CuZrO_3$ is likely a mixture of CuO and ZrO_2 phases. Collectively, our combined computational and experimental work suggests that $CuZrO_3$ is a metastable oxide that has a strong tendency to phase-segregate into CuO and ZrO_2 and if stabilized, it may not be a perovskite as previously reported, but a sandwich-like structure.

Acknowledgements

This work was supported by the National Science Foundation (NSF) grant number 1634880 (CMMI). The authors thank the University of Pittsburgh Center for Research Computing (CRC) and the NSF Extreme Science and Engineering Discovery Environment (XSEDE, ACI-1548562) for providing computational resources.

References

1. P. M. P. Berthier, *Annales de Chimie et de Physique*, 1832, 362-375.
2. M. Yoshimura and J. Livage, *MRS Bulletin*, 2011, **25**, 12-13.
3. V. B. Reddy, C. R. M. Rao and P. N. Mehrotra, *Indian J Chem A*, 1981, **20**, 81-83.
4. A. K. Sharma and N. K. Kaushik, *Thermochim Acta*, 1985, **83**, 347-376.
5. R. J. Voorhoeve, D. W. Johnson, Jr., J. P. Remeika and P. K. Gallagher, *Science*, 1977, **195**, 827-833.
6. S. Saha and S. B. Abd Hamid, *RSC Advances*, 2017, **7**, 9914-9925.
7. M. A. Ehsan, H. Khaledi, Z. Arifin and M. Mazhar, *Polyhedron*, 2015, **98**, 190-195.
8. A. V. Borhade, V. B. Gaikwad and Y. R. Baste, *Indian Journal of Applied Research*, 2013, **3**, 335-340.
9. Y. Lu, X. Liang, J. Xu, Z. Zhao and G. Tian, *Sensors and Actuators B: Chemical*, 2018, **273**, 1146-1155.
10. I. A. Fisher and A. T. Bell, *Journal of Catalysis*, 1998, **178**, 153-173.
11. N. Austin, J. Ye and G. Mpourmpakis, *Catalysis Science & Technology*, 2017, **7**, 2245-2251.
12. J. Dean, Y. Yang, N. Austin, G. Veser and G. Mpourmpakis, *ChemSusChem*, 2018, **11**, 1169-1178.
13. H. Aritani, S. Kawaguchi, T. Yamamoto, T. Tanaka, Y. Okamoto and S. Imamura, *Chemistry Letters*, 2000, **29**, 532-533.
14. Z. Liu, M. D. Amiridis and Y. Chen, *J Phys Chem B*, 2005, **109**, 1251-1255.
15. T. A. G. Restivo and S. R. H. de Mello-Castanho, *Journal of Power Sources*, 2008, **185**, 1262-1266.
16. V. B. Reddy and P. N. Mehrotra, *Thermochim Acta*, 1979, **31**, 31-37.
17. G. Kresse and J. Furthmüller, *Physical Review B*, 1996, **54**, 11169-11186.
18. G. Kresse and D. Joubert, *Physical Review B*, 1999, **59**, 1758-1775.
19. G. Hautier, C. Fischer, V. Ehrlacher, A. Jain and G. Ceder, *Inorganic Chemistry*, 2011, **50**, 656-663.
20. A. Jain, G. Hautier, C. J. Moore, S. Ping Ong, C. C. Fischer, T. Mueller, K. A. Persson and G. Ceder, *Computational Materials Science*, 2011, **50**, 2295-2310.
21. E. J. Little and M. M. Jones, *Journal of Chemical Education*, 1960, **37**, 231.
22. W. T. K. Chan and W.-T. Wong, *Polyhedron*, 2013, **52**, 43-61.
23. J. K. Burdett and S. Sevov, *Journal of the American Chemical Society*, 1995, **117**, 12788-12792.
24. K. Momma and F. Izumi, *Journal of Applied Crystallography*, 2011, **44**, 1272-1276.

25. W. Tang, E. Sanville and G. Henkelman, *Journal of Physics: Condensed Matter*, 2009, **21**, 084204.
26. G. S. Girolami, T. B. Rauchfuss, R. J. Angelici and R. J. Angelici, *Synthesis and technique in inorganic chemistry : a laboratory manual*, University Science Books, Sausalito, Calif., 1999.
27. V. M. Goldschmidt, *Naturwissenschaften*, 1926, **14**, 477-485.
28. C. J. Bartel, C. Sutton, B. R. Goldsmith, R. Ouyang, C. B. Musgrave, L. M. Ghiringhelli and M. Scheffler, *Science Advances*, 2019, **5**, eaav0693.
29. J. E. Saal, S. Kirklin, M. Aykol, B. Meredig and C. Wolverton, *JOM*, 2013, **65**, 1501-1509.
30. S. Kirklin, J. E. Saal, B. Meredig, A. Thompson, J. W. Doak, M. Aykol, S. Rühl and C. Wolverton, *Npj Computational Materials*, 2015, **1**, 15010.
31. A. R. Oganov and C. W. Glass, *The Journal of Chemical Physics*, 2006, **124**, 244704.
32. A. R. Oganov, A. O. Lyakhov and M. Valle, *Accounts Chem. Res.*, 2011, **44**, 227-237.
33. A. O. Lyakhov, A. R. Oganov, H. T. Stokes and Q. Zhu, *Computer Physics Communications*, 2013, **184**, 1172-1182.
34. J. Zhang, A. R. Oganov, X. Li, M. M. D. Esfahani and H. Dong, *Journal of Applied Physics*, 2017, **121**, 155104.
35. M. S. Kuklin and A. J. Karttunen, *The Journal of Physical Chemistry C*, 2018, **122**, 24949-24957.
36. R. Dovesi, A. Erba, R. Orlando, C. M. Zicovich-Wilson, B. Civalleri, L. Maschio, M. Rérat, S. Casassa, J. Baima, S. Salustro and B. Kirtman, *WIREs Computational Molecular Science*, 2018, **8**, e1360.
37. J. P. Perdew, M. Ernzerhof and K. Burke, *The Journal of Chemical Physics*, 1996, **105**, 9982-9985.
38. Q.-L. Tang, Q.-J. Hong and Z.-P. Liu, *Journal of Catalysis*, 2009, **263**, 114-122.
39. Q.-J. Hong and Z.-P. Liu, *Surface Science*, 2010, **604**, 1869-1876.
40. W. Guan, S. Long, Q. Liu, M. Liu and W. Wang, *IEEE Electron Device Letters*, 2008, **29**, 434-437.
41. C. V. Reddy, I. N. Reddy, K. Ravindranadh, K. R. Reddy, N. P. Shetti, D. Kim, J. Shim and T. M. Aminabhavi, *Journal of Environmental Management*, 2020, **260**, 110088.
42. Y. Sun and P. A. Sermon, *Topics in Catalysis*, 1994, **1**, 145-151.